



HAL
open science

Blueschist-facies metapelites from the Malpica-Tui Unit (NW Iberian Massif): phase equilibria modelling and H₂O and Fe₂O₃ influence in high-pressure assemblages

A. Lopez-Carmona, Pavel Pitra, J. Abati

► **To cite this version:**

A. Lopez-Carmona, Pavel Pitra, J. Abati. Blueschist-facies metapelites from the Malpica-Tui Unit (NW Iberian Massif): phase equilibria modelling and H₂O and Fe₂O₃ influence in high-pressure assemblages. *Journal of Metamorphic Geology*, 2013, 31 (3), pp.263-280. 10.1111/jmg.12018 . insu-00797428

HAL Id: insu-00797428

<https://insu.hal.science/insu-00797428>

Submitted on 4 Mar 2021

HAL is a multi-disciplinary open access archive for the deposit and dissemination of scientific research documents, whether they are published or not. The documents may come from teaching and research institutions in France or abroad, or from public or private research centers.

L'archive ouverte pluridisciplinaire **HAL**, est destinée au dépôt et à la diffusion de documents scientifiques de niveau recherche, publiés ou non, émanant des établissements d'enseignement et de recherche français ou étrangers, des laboratoires publics ou privés.

Blueschist-facies metapelites from the Malpica–Tui Unit (NW Iberian Massif): phase equilibria modelling and H₂O and Fe₂O₃ influence in high-pressure assemblages

A. LÓPEZ-CARMONA, P. PITRA AND I. ABATI

ABSTRACT The Malpica–Tui Unit (Galicia, NW Spain) records eclogite- and blueschist-facies metamorphism during the onset of the Variscan orogeny in Europe. Petrological analysis involving pseudosections calculated using THERMOCALC shows that the Upper Sheet of this unit, the Ceán Schists, recorded a three-stage metamorphic evolution involving (i) Early subduction-related medium-pressure/low-temperature metamorphism (M₁) constrained at ~350–380 °C, 12–14 kbar, which is only recorded in the basal part (lower metapelites, LM) of the Ceán Schists. (ii) Subduction-related blueschist facies prograde metamorphism (M₂) going from ~19 kbar, 420 °C to 21 kbar, 460 °C in the LM, and from 16 kbar 430 °C to 21–22 kbar, 520 °C in the structurally upper metapelites (UM). (iii) Exhumation-related metamorphism (M₃) is characterized by a decompression to 8–10 kbar, 470–490 °C in the LM. This decompression is also recorded in the UM, but it was not possible to estimate precise *P–T* conditions. The calculations indicate that (i) the prograde evolution in subduction zones may occur in fluid-undersaturated conditions due to the crystallization of lawsonite, even in metapelitic rocks. This significantly influences phase equilibria and hence the *P–T* estimates. (ii) The proportion of ferric iron also has a strong influence on phase equilibria, even in metapelites. However, the analysed values of Fe₂O₃ may not reflect the oxidation state during the main metamorphic evolution and are probably easily modified by superficial alteration even in apparently fresh samples. The use of *P–T–X*(Fe₂O₃) pseudosections together with petrographic observations is then necessary to estimate the real oxidation state of the rocks and correctly evaluate the *P–T* conditions.

Key words: blueschist-facies metapelites, H₂O content, Iberian Massif, MnNCKFMASHTO, Variscan subduction

INTRODUCTION

Sinking of cold, dense lithosphere in subduction zones is the principal plate-driving force, causing orogenesis along continental margins. The descent of a relatively cold crustal slab to mantle depths leads to the formation of high-pressure (HP) and low- (LT) to medium-temperature (MT) metamorphic rocks, like blueschists and eclogites, frequently found in the suture zones of orogenic belts (e.g. Miyashiro, 1961; Ernst, 1971; Maruyama *et al.*, 1996). Blueschist- and eclogite-facies assemblages, as markers of fossil and active subduction zones, store much information concerning processes at convergent plate boundaries, and provide important clues to the understanding of the thermal history of the evolving Earth (e.g. Ernst, 1973, 2001; Platt, 1993; Stern, 2005).

Data about the metamorphic evolution of subducted terranes, obtained through petrological analysis and thermodynamic modelling, are fundamental to geodynamic models and palaeogeographical reconstructions of the lithospheric plates. In this context, the northwest section of the Iberian Massif provides

information that helps to understand the evolution of the European Variscan belt. This region comprises exotic terranes forming a huge and complex allochthonous sheet emplaced upon the sequences deposited on the passive margin of north Gondwana (Martínez Catalán *et al.*, 2009). They include a HP and LT MT belt that can be discontinuously traced throughout the Variscan belt, located below several rock units with ophiolitic associations, probably having originated in the Rheic Ocean. This HP belt is a coherent piece of continental crust formed by different rock units known in the NW Iberian Massif as the Basal Units (Fig. 1). The goal of this work is to analyse phase equilibria of blueschist-facies metapelites (Ceán Schists) from the upper sequence of the westernmost basal unit, the Malpica Tui Unit (MTU; Fig. 1), with particular attention to the effects of H₂O and Fe₂O₃. This lithology preserves the chloritoid glaucophane paragenesis (López-Carmona *et al.*, 2010), which is one of the classic HP indicators in metapelites (e.g. Kiénaest & Triboulet, 1972; Katagas, 1980; Chopin, 1981; El-Shazly & Liou, 1991; Wei & Song, 2008).

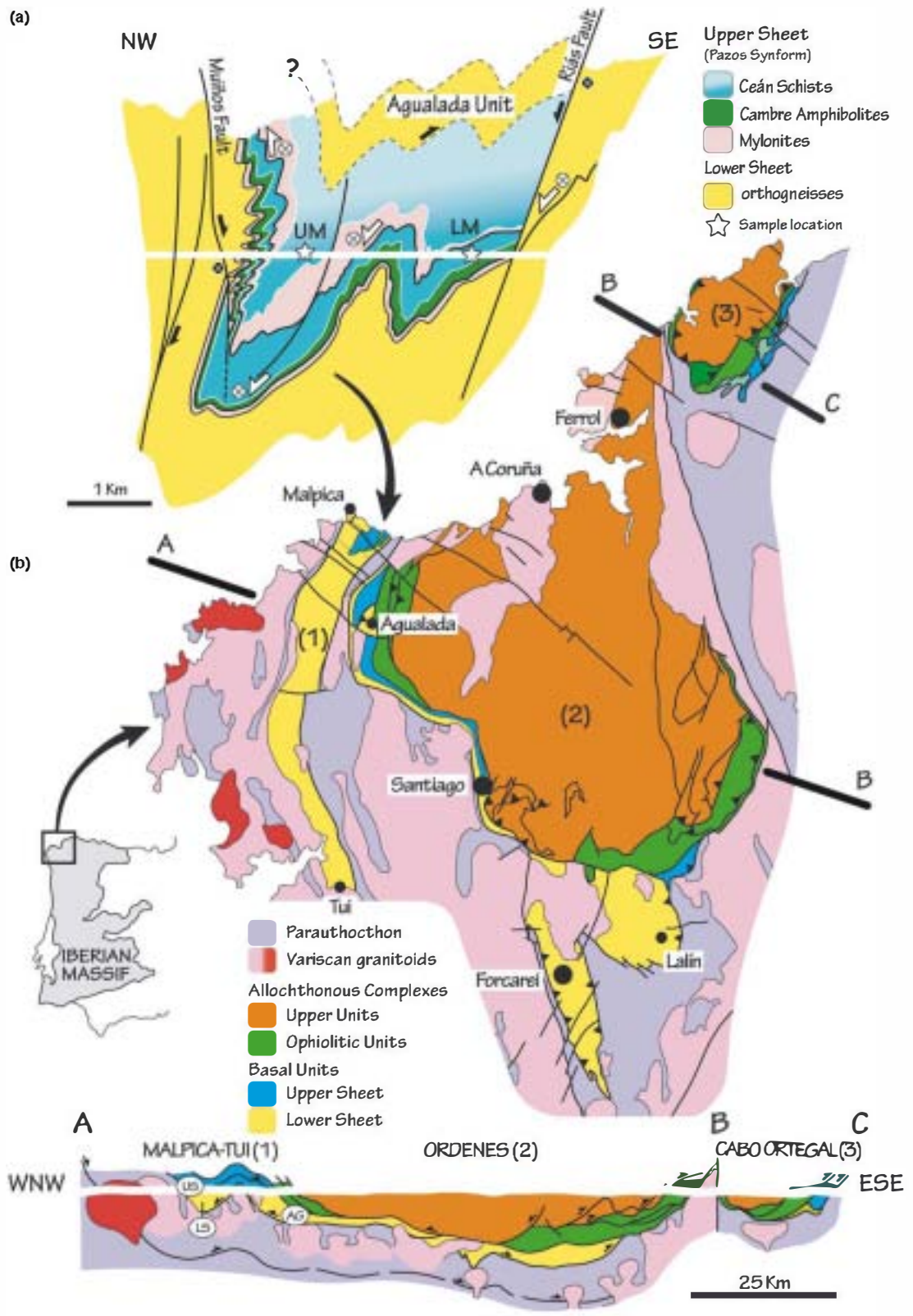


Figure 1. (a) Cross-section for the Upper Sheet (Pazos Synform) of the Malpica Tui Unit. The gradation of colours indicates the decrease in the metamorphic grade. Sample locations are indicated. Modified from Díez Fernández (2011). (b) Geological map of the Allochthonous Complexes of the NW Iberian Massif. A B and B C correspond to cross-sections along the different units. US, upper sheet; LS, lower sheet; AG, Agualada Unit. Modified from Martínez Catalán *et al.* (2009).

Phase equilibria of pelitic rocks at high pressures do not attract as much attention as metabasic rocks, probably because the mineral associations are less spectacular. Yet, metapelitic rocks are common in HP terranes (e.g. Bosse *et al.*, 2002; Wei & Powell, 2003 and references therein), and are suitable for constraining P - T evolution. However, similar to metabasic rocks, the assemblages are sensitive to the amount of available H_2O and Fe_2O_3 (cf. Korhonen *et al.*, 2012).

HIGH-PRESSURE ROCKS IN THE BASAL UNITS OF NW IBERIA

Pods and relicts of HP rocks, well preserved in the NW Iberian massif, with widespread distribution along the so-called Basal Units, are the best record of the Variscan subduction of the north Gondwana margin during the Late Devonian. Their petrological and structural study has constrained the P - T paths and the kinematics of the subduction (e.g. Martínez Catalán *et al.*, 1996; Arenas *et al.*, 1997; López-Carmona *et al.*, 2010; Díez Fernández *et al.*, 2011), concluding that Basal Units formed part of a subducting slab buried beneath Laurussia at the onset of the Variscan collision (Arenas *et al.*, 1995, 1997; Santos Zalduegui *et al.*, 1995; Rodríguez Aller *et al.*, 2003; Abati *et al.*, 2010). They were rapidly exhumed by crustal-scale thrusting accompanied by recumbent folding and tectonic denudation (Martínez Catalán *et al.*, 1996, 1997; Díez Fernández & Martínez Catalán, 2009; Díez Fernández *et al.*, 2011). The original polarity of the subducting slab was reconstructed on the basis of the palaeo-pressures inferred from metamorphic parageneses, indicating that the subduction had a significant westward component in present coordinates (Martínez Catalán *et al.*, 1996). Kinematic indicators in HP fabrics are in agreement with this reconstruction, indicating top to the northwest movement (Díez Fernández *et al.*, 2012).

According to their metamorphism and tectonostratigraphy, the Basal Units can be separated into two sheets (Fig. 1). In the MTU: (i) a Lower Sheet of continental affinity, where felsic orthogneisses and turbiditic metasedimentary rocks predominate; and (ii) an Upper Sheet that represents a volcano-sedimentary sequence viewed as a more distal part of the same continental margin, extremely attenuated and transitional to an oceanic domain (Rodríguez Aller, 2005). The Upper Sheet is preserved in a small synformal structure (the Pazos Synform) and is formed by a basal layer of finely foliated amphibolites and greenschists with N-MORB chemistry (Cambre Amphibolites), and an overlying sequence of pelitic schists (Ceán Schists) with minor intercalations of bituminous schist, cherts and carbonates. The mafic rocks are strongly retrogressed blueschists that locally preserve lawsonite pseudomorphs dominated by epidote/clinozoisite and paragonite (Rodríguez Aller *et al.*, 2003; López-Carmona *et al.*, 2010). The contact between the Upper and

the Lower Sheets is marked by a several metres thick layer of mylonites and ultramylonites located at the base of the Cambre Amphibolites (Díez Fernández, 2011). Another layer of mylonites occurs in the middle of the Upper Sheet, within the Ceán Schists, separating them in a lower and an upper part (Fig. 1a).

Peak metamorphic conditions in the Lower Sheet of the MTU are in the intermediate temperature eclogite facies (Rodríguez *et al.*, 2005), with a progressive transition to the blueschist facies in the eastern sections of the same units in the remaining allochthonous complexes (Martínez Catalán *et al.*, 1996; Rubio Pascual *et al.*, 2002). The Upper Sheet can be considered as a highly condensed metamorphic sequence with a lower part in the blueschist facies and an uppermost part without HP relicts (Fig. 1a). The significant difference in metamorphic grade between the Upper and the Lower Sheets, and between the upper and lower part of the Upper Sheet suggests that the mylonites that mark the contacts are related to extensional deformation (López-Carmona *et al.*, 2007; Fig. 1).

Previous P - T estimates

The metamorphic evolution of the Ceán Schists has been previously studied by conventional thermobarometric techniques, multiequilibrium thermobarometry (THERMOCALC average P - T) and thermodynamic modelling, using pseudosections in the KFMASH and MnNCKFMASH chemical systems (López-Carmona *et al.*, 2010). Conventional thermobarometry calculations using microinclusion compositions indicate peak conditions of ~ 19 – 22 kbar and 500 °C. The same calculations using the matrix minerals yield approximate values of 16 – 20 kbar and 440 – 515 °C. P - T values obtained with the average P - T multiequilibrium thermobarometry are compatible with the conventional thermobarometry results, but show significantly lower pressures for the matrix foliation (13 – 14 kbar and 495 – 500 °C). Petrological modelling in the MnNCKFMASH system provided a minimum pressure limit for the paragenesis chloritoid + glaucophane at ~ 17 kbar, confirming the HP stability of this assemblage.

SAMPLE DESCRIPTION AND MINERAL CHEMISTRY

The deformation in the Ceán Schists is relatively heterogeneous, with irregular development of foliations and deformation phases in different domains. Their deformation history includes several compressive, extensional and strike-slip phases (Díez Fernández *et al.*, 2011). However, only three of the deformation phases have a direct link with relevant metamorphic associations. Two blueschist facies deformation phases have been identified (D_1 – D_2), followed by the development of the main foliation in blueschist-amphibolite facies conditions (D_3) and an amphibolite greenschist facies overprint (post- D_3) (Fig. 2). The fabric from the

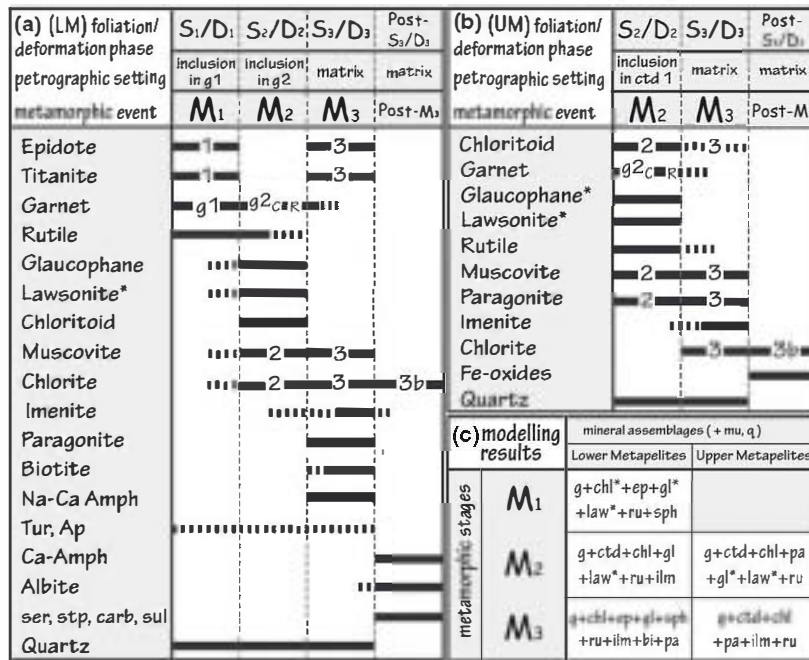


Figure 2. Diagram showing the crystallization-deformation relations of the Ceán Schists in the lower (a) and upper metapelites (b). (c) Summary of the modelling results showing the mineral assemblages predicted in the metamorphic events. *Inferred phases that have not been observed petrographically.

Table 1. (a) Bulk-rock composition from XRF analyses of samples LM and UM expressed in wt%. (b) Bulk-rock compositions normalized with THERMOCALC expressed in mol%. Fe₂O_{3(T)} was measured by the XRF and FeO by wet chemical titration. The amount Fe₂O₃ is calculated stoichiometrically as: [total iron/1.43 (FeO/1.286)*1.43].

Studied samples	MnNCKFMASH \bullet				CKFMASH				
	LM (wt%)	UM (wt%)	LM (mol. %)	UM (mol. %)	UM (mol. %)				
(a)		(b)							
SiO ₂	57.54	57.67	SiO ₂	66.15	66.15	68.63	68.63	49.73	81.04
TiO ₂	1.01	0.74	TiO ₂	0.87	0.87	0.66	0.66	0.53	
Al ₂ O ₃	17.04	20.96	Al ₂ O ₃	11.55	11.55	14.70	14.70	7.17	8.66
FeO	6.78	5.93	FeO	7.72	7.72	7.68	7.68	2.01	3.02
Fe ₂ O ₃	1.39	1.98		0.60	0.60	0.89	0.05	0.04	
MnO	0.17	0.26	MnO	0.17	0.17	0.26	0.26	0.01	
MgO	2.92	1.72	MgO	5.00	5.00	3.05	3.05	1.68	3.03
CaO	2.75	0.36	CaO	3.16	3.16	0.24	0.24	0.04	0.07
Na ₂ O	1.26	0.85	Na ₂ O	1.40	1.40	0.98	0.98	0.79	
K ₂ O	4.59	3.83	K ₂ O	3.37	3.37	2.91	2.91	2.33	4.19
P ₂ O ₅	0.14	0.13	H ₂ O	In excess	14.38	In excess	In excess	35.69	In excess
Cr ₂ O ₃	0.05	0.04	Figure	5a;5c	5b;5d	6a;6c	6d	6e	6f

earliest deformational event (S₁) is preserved exclusively as inclusion trails in a first generation of garnet porphyroblasts. S₂ is preserved in a second generation of garnet and chloritoid porphyroblasts. The matrix foliation (S₃) usually obliterates the previous fabric, resulting in a composite foliation S₂ + S₃ and includes the pervasive development of spaced extensional shear bands and meso-scale folds, related with a first extensional event (Díez Fernández *et al.*, 2011). Subsequent deformations are associated with the development of late-Variscan folds (such as Pazos Synform, Fig. 1) and to a final superposed dextral strike-slip

tectonics. The effects of post-S₃ deformations associated with vertical folding are particularly evident in the core of the synformal structure, where an axial-planar foliation S₄ is usually developed. In these areas, the schists are highly altered and the main foliation consists of alternations of quartz and phyllosilicate-rich layers.

The dominant rock type of the Ceán series is a typical pelite (e.g. Atherton & Brotherton, 1982). However, to the base of the sequence, metapelitic rocks are interbedded with the Cambre Amphibolites and most samples show compositions that move away from the field of pure pelites in the direction of N-MORB, indicating either some mixing between both lithologies during primary volcano-sedimentary processes, or mechanical assimilation during the deformation. The different whole-rock chemistry between the samples selected for this study results in slightly different mineral associations (Table 1).

The Ceán Schists show a medium-grained porphyro lepidoblastic texture and a well-developed planar to planar linear fabric (Fig. 3). White mica and quartz constitute > 50%, and locally up to 80%, of the modal proportion of each sample. The alternation of both minerals defines a banding preserved between extensional shear bands. The foliation is defined by the shape preferred orientation of phengitic muscovite, paragonite and chlorite, and is parallel to the banding. Quartz grains commonly show undulate extinction, subgrain boundaries and recrystallization to smaller grain aggregates (Fig. 3).

Two representative samples of the Ceán Schists from the Upper Sheet of the MTU (Fig. 1) were studied. Sample 106340, referred to hereafter as LM

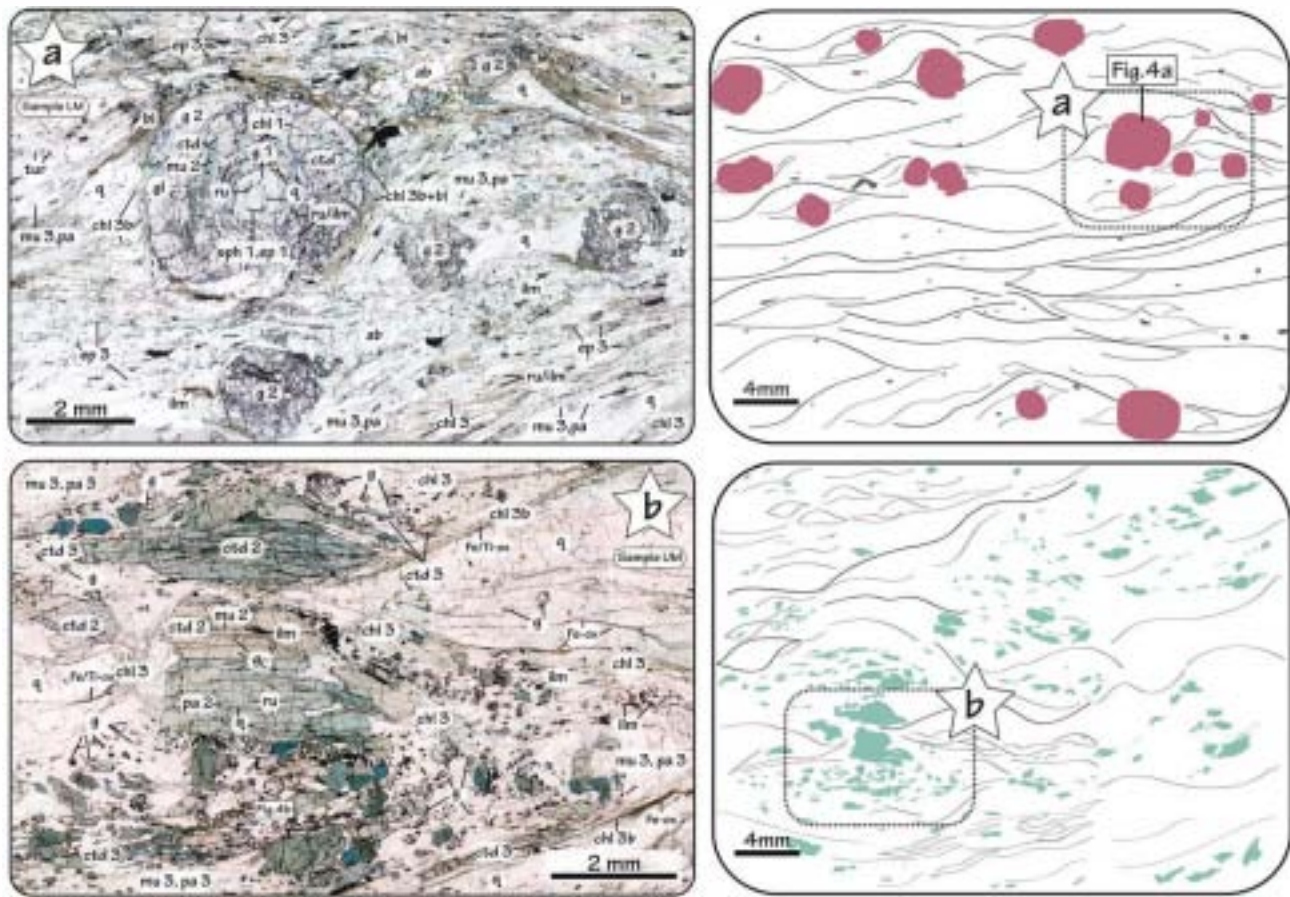


Figure 3. Microphotographs of the Ceán Schists. Photomontages of thin-section images displaying the porphyro lepidoblastic texture and the highly deformed fabrics. (a) Sample LM showing garnet porphyroblasts filled with concentric inclusions. (b) Sample UM cluster of highly pleochroic chloritoid porphyroblasts and numerous small garnets. Sample locations are indicated in Fig. 1. Mineral abbreviations are after Holland & Powell (1998). Other abbreviations: tur, tourmaline; Fe/Ti-ox, Fe/Ti-bearing oxides.

(for lower metapelites), is located at the base of the synformal structure, and interbedded within the Cambre Amphibolites. The presence of numerous garnet porphyroblasts rich in S_1 and S_2 inclusions makes this sample ideal to study the first subduction-related deformation phases. Sample 108289, referred to hereafter as UM (for upper metapelites), is located structurally above the sample 106340, in the middle part of the synformal structure, in an upper structural domain separated from the first by a mylonitic band (Fig. 1a).

Mineral analyses and elemental X-ray maps have been performed with a JEOL-Superprobe JXA-8900M microprobe equipped with five spectrometers at the ICTS-National Electronic Microscopy Centre at the Complutense University of Madrid (Spain; <http://www.cnme.es>). The operating parameters for punctual analyses were 15 kV accelerating voltage, 20 nA beam current, between 1 and 5 μm beam diameter (1 μm for the microinclusions) and 10 s counting time. X-ray maps were operated at 20 kV and 150 nA. Representative analyses of selected minerals are listed in

Tables 2 and 3. Mineral abbreviations are those used by THERMOCALC (Holland & Powell, 1998): albite (ab), biotite (bi), chlorite (chl), chloritoid (ctd), clinzoisite (cz), epidote (ep), garnet (g), glaucophane (gl), ilmenite (ilm), jadeite (jd), lawsonite (law), muscovite (mu), omphacite (o), paragonite (pa), plagioclase (pl), quartz (q), rutile (ru) and titanite (sph). Other abbreviations: apatite (ap), barroisite (bar), carbonates (carb), Fe/Ti-bearing oxides (Fe/Ti-ox), hornblende (hb), sericite (ser), stilpnomelane (stp), sulphides (sul), tschermakite (ts), tourmaline (tur) and winchite (win). Other symbols: $X_{\text{Fe}} = \text{Fe}^{2+}/(\text{Fe}^{2+} + \text{Mg})$; $X_{\text{Fe}^{3+}} = \text{Fe}^{3+}/(\text{Fe}^{3+} + \text{Al}_2)$ (epidote); $X_{\text{Fe}^{3+}} = \text{Fe}^{3+}/(\text{Fe}^{3+} + \text{Al})$ (amphibole); $X_{\text{Na}} = \text{Na}/(\text{Na} + \text{K})$ (white mica); $X_{\text{Na}} = \text{Na}/(\text{Na} + \text{Ca})$ (amphibole); Alm = $\text{Fe}/(\text{Fe} + \text{Mg} + \text{Ca} + \text{Mn})$, Prp = $\text{Mg}/(\text{Fe} + \text{Mg} + \text{Ca} + \text{Mn})$, Grs = $\text{Ca}/(\text{Fe} + \text{Mg} + \text{Ca} + \text{Mn})$, Sps = $\text{Mn}/(\text{Fe} + \text{Mg} + \text{Ca} + \text{Mn})$; per formula unit (pfu); weight per cent (wt%); ‘ \rightarrow ’ denotes core-to-rim evolution, and ‘*’ indicates phases inferred from the petrological modelling that have not been identified petrographically.

Table 2. Representative microprobe analyses from sample LM.

Mineral	S ₁				S ₂					S ₃					Post-S ₃								
	ep 1	sph 1	g 1c	g 1p	g 1	ctd	mu 2	chl 2	g2c	g2p	ilm	ep 3	mu 3	bi	pa	chl 3	sph 3	win	bar	chl 3b	hb	ts	sl
Analysis	9	1	2	196	2	3	160	43	179	183	18	18	4	13	39	67	8	11	26	95	17	24	85
SiO ₂	38.13	30.46	36.98	37.36	56.79	23.81	51.29	25.93	37.47	37.92	0.05	38.04	50.92	36.54	46.70	24.61	30.16	53.96	46.75	24.52	44.94	47.23	67.25
TiO ₂	0.04	35.81	0.31	0.05	0.03	0.02	0.15	0.07	0.12	0.09	53.38	0.15	0.19	1.55	0.07	0.06	35.51	0.14	0.10	0.09	0.26	0.23	0.00
Al ₂ O ₃	26.26	1.41	20.81	22.08	11.78	39.06	24.73	21.23	22.16	22.01	0.34	26.68	27.44	16.71	39.38	23.15	1.83	13.28	9.43	22.50	12.74	10.40	19.87
Cr ₂ O ₃	0.11	0.03	0.01	0.05	0.01	0.05	0.06	0.04	0.00	0.03	0.08	0.09	0.05	0.10	0.00	0.00	0.00	0.04	0.00	0.01	0.04	0.12	0.00
Fe ₂ O ₃	11.07	0.00	0.82	0.00	0.98	1.97	1.19	0.00	0.00	0.00	0.00	9.75	0.00	0.00	0.05	0.00	0.00	3.61	6.05	0.00	5.61	4.51	0.03
FeO	0.10	0.76	22.46	27.51	11.86	22.27	3.17	21.82	23.61	27.06	42.24	0.09	3.51	18.36	1.09	29.14	1.23	14.01	11.99	27.72	11.63	11.93	0.00
MnO	0.19	0.18	7.95	2.46	0.04	0.36	0.00	0.15	4.55	1.66	3.75	0.08	0.03	0.18	0.01	0.41	0.32	0.47	0.42	0.26	0.45	0.51	0.03
MgO	0.00	0.00	0.54	0.88	10.04	3.20	3.33	16.44	0.56	0.80	0.00	0.04	2.35	11.57	0.25	10.84	0.00	7.32	11.29	12.00	10.74	11.20	0.00
CaO	22.21	30.06	10.03	8.37	0.41	0.01	0.03	0.04	10.24	9.36	0.00	23.20	0.00	0.00	0.05	0.00	29.40	6.14	8.88	0.08	10.19	9.80	0.06
Na ₂ O	0.00	0.02	0.05	0.03	6.43	0.03	0.22	0.03	0.00	0.03	0.00	0.02	0.28	6.02	0.01	0.04	1.63	2.40	0.01	1.59	1.77	10.92	
K ₂ O	0.00	0.02	0.00	0.00	0.02	0.00	9.73	0.02	0.00	0.01	0.01	0.02	10.20	9.79	2.23	0.01	0.00	0.62	0.25	0.06	0.37	0.30	0.03
Total	98.11	98.75	99.96	98.8	98.39	90.78	93.90	85.77	98.71	98.97	99.85	98.16	94.97	94.82	95.91	88.23	98.49	101.2	97.56	87.25	98.56	98.00	98.19
Si	2.99	1.01	2.97	3.00	7.81	1.00	3.48	2.74	3.00	3.03	0.00	2.98	3.42	2.79	2.99	2.63	1.25	7.42	6.88	2.63	6.54	6.88	2.98
Ti	0.00	0.90	0.02	0.00	0.00	0.00	0.01	0.01	0.01	0.01	1.01	0.01	0.01	0.09	0.00	0.00	0.00	0.01	0.01	0.01	0.03	0.03	0.00
Al	2.43	0.06	1.97	2.09	1.91	1.94	1.98	2.64	2.09	2.07	0.01	2.46	2.17	1.50	2.97	2.91	0.84	2.15	1.62	2.85	2.19	1.79	1.04
Cr	0.01	0.00	0.00	0.00	0.00	0.00	0.00	0.00	0.00	0.00	0.00	0.00	0.00	0.00	0.00	0.00	0.00	0.00	0.00	0.00	0.00	0.01	0.00
Fe ³⁺	0.65	0.00	0.05	0.00	0.10	0.06	0.06	0.00	0.00	0.00	0.00	0.57	0.00	0.00	0.00	0.00	0.89	0.37	0.67	0.00	0.61	0.49	0.00
Fe ²⁺	0.01	0.02	1.51	1.85	1.37	0.78	0.18	1.93	1.58	1.81	0.89	0.01	0.19	1.17	0.06	2.60	0.00	1.61	1.48	2.49	1.42	1.45	0.00
Mn	0.01	0.01	0.54	0.17	0.01	0.01	0.00	0.01	0.31	0.11	0.08	0.01	0.00	0.01	0.00	0.04	0.05	0.06	0.05	0.02	0.06	0.06	0.00
Mg	0.00	0.00	0.06	0.11	2.06	0.20	0.34	2.59	0.07	0.10	0.00	0.00	0.23	1.32	0.02	1.72	0.09	1.50	2.45	1.92	2.33	2.43	0.00
Ca	1.87	1.07	0.86	0.72	0.06	0.00	0.00	0.01	0.88	0.80	0.00	1.95	0.00	0.00	0.00	0.00	0.20	0.91	1.38	0.01	1.59	1.52	0.00
Na	0.00	0.00	0.01	0.01	1.72	0.00	0.03	0.01	0.00	0.01	0.00	0.00	0.04	0.00	0.75	0.00	0.00	0.44	0.68	0.00	0.45	0.50	0.94
K	0.00	0.00	0.00	0.00	0.00	0.00	0.84	0.00	0.00	0.00	0.00	0.00	0.87	0.95	0.18	0.00	0.00	0.11	0.05	0.01	0.07	0.06	0.00
Sum	7.97	3.06	8.00	7.95	15.04	3.99	6.92	9.94	7.94	7.93	1.99	7.99	6.93	7.83	6.97	9.90	3.33	14.58	15.26	9.94	15.29	15.22	4.96
X _{Fe}			0.96	0.95	0.40	0.80	0.35	0.43	0.96	0.95		0.45	0.47	0.75	0.60		0.52	0.38	0.56	0.38	0.37		
X _{Na}					0.97		0.03						0.04				0.32	0.33		0.22	0.25		
X _{Fe3+}	0.60				0.05	0.03						0.55					0.15	0.29		0.22	0.21		

C, core; R, rim. Data calculated using AX software (Holland & Powell, 2000 in Powell & Holland 2002 <http://www.esc.cam.ac.uk/research/research-groups/holland/ax>). The amount of ferric iron was calculated from stoichiometric constraints using the programme AX (Powell & Holland, 2002). For amphibole, the Fe3+ content corresponds to the average from minimum and maximum constraints (Holland & Blundy, 1994).

Table 3. Representative microprobe analyses from sample UM.

Mineral	S ₂					S ₃					Post-S ₃	
	mu 2	mu 2	ctd 2	INCL	MTX	ep	mu 3	mu 3	ctd 3	chl 3	ilm	chl 3b
Analysis	33	100	134	116	82	70	52	53	40	35	4	13
SiO ₂	49.98	46.55	24.28	37.00	37.26	38.24	49.15	47.45	24.51	24.14	0.05	23.92
TiO ₂	0.15	0.07	0.06	0.13	0.09	0.02	0.24	0.09	0.02	0.07		53.37
Al ₂ O ₃	28.09	39.36	41.69	20.35	20.72	21.29	28.10	40.29	41.24	23.00	0.00	23.27
Cr ₂ O ₃	0.02	0.06	0.05	0.00	0.04	0.03	0.00	0.00	0.00	0.00	0.00	0.05
Fe ₂ O ₃	1.81	0.00	0.00	0.00	0.00	0.00	1.18	0.23	0.50	0.00	0.00	0.10
FeO	4.14	0.96	22.18	24.26	18.76	31.44	3.98	0.86	23.35	29.84	42.34	29.31
MnO	0.05	0.01	0.15	11.20	16.54	2.55	0.00	0.04	0.34	0.23	3.11	0.32
MgO	2.75	0.07	2.30	1.14	0.57	1.70	2.52	0.09	3.16	11.05	0.00	12.05
CaO	0.00	0.12	0.00	6.06	6.98	5.08	0.01	0.05	0.00	0.02	0.00	0.02
Na ₂ O	0.29	6.84	0.01	0.04	0.01	0.05	0.44	6.71	0.00	0.00	0.00	0.00
K ₂ O	10.48	0.58	0.03	0.00	0.00	0.00	10.16	0.82	0.00	0.00	0.00	0.03
Total	97.76	94.62	90.75	100.18	100.97	100.40	95.78	96.66	93.42	88.35	98.87	89.21
Si	3.33	3.00	1.01	2.99	2.99	3.05	3.32	2.99	1.00	2.59	0.00	2.53
Ti	0.01	0.00	0.00	0.01	0.01	0.00	0.01	0.00	0.00	0.01	1.02	0.01
Al	2.21	2.99	2.04	1.94	1.96	2.00	2.24	3.00	1.98	2.91	0.00	2.91
Cr	0.00	0.00	0.00	0.00	0.00	0.00	0.00	0.00	0.00	0.00	0.00	0.00
Fe ³⁺	0.09	0.00	0.00	0.08	0.06	0.00	0.06	0.01	0.03	0.00	0.00	0.01
Fe ²⁺	0.14	0.05	0.77	1.56	1.20	2.09	0.16	0.04	0.50	2.67	0.90	2.60
Mn	0.00	0.00	0.01	0.77	1.12	0.17	0.00	0.00	0.01	0.02	0.07	0.03
Mg	0.27	0.01	0.14	0.14	0.07	0.20	0.25	0.01	0.19	1.76	0.00	1.91
Ca	0.00	0.01	0.00	0.52	0.60	0.43	0.00	0.01	0.00	0.00	0.00	0.00
Na	0.04	0.85	0.00	0.01	0.00	0.01	0.06	0.82	0.00	0.00	0.00	0.00
K	0.89	0.05	0.00	0.00	0.00	0.00	0.88	0.07	0.00	0.00	0.00	0.00
Sum	6.98	6.96	3.97	8.00	8.00	7.96	6.99	6.94	4.00	9.96	1.98	10.00
X _{Fe}	0.34	0.88	0.84	0.92	0.95	0.91	0.39	0.81	0.60	0.81	0.58	0.58
X _{Fe3+}			0.84						0.81			
X _{Na}	0.04	0.95					0.06	0.93				

C, core; R, rim; INCL, inclusion in ctd 2; MTX, matrix. Data calculated using AX software (Holland & Powell, 2000 in Powell & Holland 2002 <http://www.esc.cam.ac.uk/research/research-groups/holland/ax>). The amount of ferric iron was calculated from stoichiometric constraints using the programme AX (Powell & Holland, 2002). For amphibole, the Fe3+ content corresponds to the average from minimum and maximum constraints (Holland & Blundy, 1994).

Structurally lower metapelites

Sample LM is a micaschist that contains a main foliation (S_3) defined by white mica (type 3 phengite with 3.40–3.45 Si pfu, $X_{Na} = 0.04$ and paragonite, $X_{Na} = 0.81$), biotite ($X_{Fe} = 0.47$), epidote (type 3; $X_{Fe^{3+}} = 0.55$), minor chlorite (type 3; $X_{Fe} = 0.60$) and quartz. The dominant Ti-bearing minerals in the matrix are Mn-rich ilmenite (MnO = 3.7 wt%, i.e. ~9% pyrophanite) and titanite (type 3), which contains up to 1.8 wt% Al_2O_3 , up to 1.2 wt% FeO and up to 0.4 wt% F. S_3 parageneses also include minor proportions of bluish Ca Na amphiboles such as winchite (Si = 7.4 pfu; $X_{Na} = 0.30$ 0.32; $X_{Fe} = 0.51$ 0.52) and barroisite (Si = 6.9 pfu; $X_{Na} = 0.33$ 0.36; $X_{Fe} = 0.45$ 0.5), and relatively abundant small crystals of dravite-rich tourmaline and apatite (Fig. 3a; Table 2).

This foliation wraps around subhedral crystals of garnet (0.5–4 mm) concentrated in the micaceous domains of the matrix, and locally included in albite porphyroblasts. Garnet is rich in inclusions, which commonly display a concentric arrangement (Figs 3a & 4a). Locally, however, they define curved or sigmoidal patterns or, more rarely, markedly rotational paths arranged as spirals (snowball garnet). Large garnet crystals display an optical zoning. The cores, referred to as garnet 1 (g1), usually lack fractures and contain very fine-grained inclusions (<0.06 mm) of epidote (type 1, $X_{Fe^{3+}} = 0.60$), titanite (type 1), rutile needles and quartz (Fig. 3a; Table 2). In general, the inclusions define a very fine foliation, S_1 . The outer parts of large garnet, referred to as garnet 2 (g2), are commonly fractured and rich in coarser-grained (up to 0.7 mm) inclusions of glaucophane (Si = 7.8 pfu; $X_{Na} = 0.97$; $X_{Fe} = 0.4$; $X_{Fe^{3+}} = 0.05$ 0.1), chloritoid ($X_{Fe} = 0.80$), phengitic muscovite (type 2, Si up to 3.5 pfu) that is locally also included in chloritoid (an inclusion in an inclusion), chlorite (type 2, $X_{Fe} = 0.43$), rutile (locally partly replaced by ilmenite), ilmenite and quartz (Fig. 3a; Table 2). In most cases, these inclusions define a curved or sigmoidal foliation (S_2) discordant with the external foliation, S_3 . The optical zoning can be correlated with the chemical zoning (Fig. 4a). Type 1 garnet core displays zoning characterized by an increase in almandine and pyrope (Alm51 → 60, Prp2 → 3) and a decrease in spessartine (Sps18 → 9). X_{Fe} remains constant ($X_{Fe} = 0.96$) and the proportion of grossular varies irregularly between 28 and 31%. The apparent absence of zoning in garnet 1 core in Fig. 4a is caused by the profile running slightly off the centre of the crystal; the core values were obtained by point analysis (Table 2). The garnet 1 zoned rim (Fig. 4a; profile 1) is characterized by an increase in the amount of both grossular and spessartine, compensated by the decrease of the proportion of almandine (Grs28 → 32, Sps9 → 11, Alm61 → 55). In type 2 garnet, the rimward evolution is characterized by a decrease in grossular, spessartine

and X_{Fe} (Grs31 → 19, Sps11 → 1, $X_{Fe} = 0.96$ → 0.93), accompanied by an increase in almandine and pyrope (Alm55 → 73, Prp3 → 6).

Finally, post- S_3 minerals are locally present around garnet and are commonly composed by intergrowths of chlorite (type 3b), albite and quartz. Garnet rim is nearby replaced by chlorite flakes (type 3b; $X_{Fe} = 0.56$). Rare bluish-green Ca-amphibole such as Fe/Mg-hornblende (Si = 6.5–6.8 pfu; $X_{Na} = 0.17$ 0.22; $X_{Fe} = 0.51$ 0.38; $X_{Fe^{3+}} = 0.07$ 0.22) and tschermakite (Si = 6.9 pfu; $X_{Na} = 0.24$ 0.25; $X_{Fe} = 0.36$ 0.37; $X_{Fe^{3+}} = 0.21$) grow in optical continuity on the rims of the Na Ca amphibole. Locally, hornblende develops large crystals (>0.3 mm long), which are arranged parallel to type 3b chlorite (Fig. 3a; Table 2). Minor proportions of sericite, stilpnomelane, carbonates and sulphides are commonly concentrated along the extensional shear planes and in some samples a pervasive growth of albite porphyroblasts occurs.

In summary, three metamorphic stages (M_1 – M_3) can be distinguished in the evolution of this sample (Fig. 2). Evidence for M_1 is recorded by aligned inclusions (ep, ru, sph, q) in the cores of large garnet (g1) (Fig. 3a). M_2 is characterized by the inclusions of ctd, chl, gl, ru, ilm, mu, q preserved in garnet 2. The third stage (M_3) is recorded by the matrix foliation (S_3), comprising the assemblage chl-ep-mu-pa-bi-ru/ilm-sph-q ± g ± win/bar (Figs 2a & 3a). Finally, post- M_3 crystallization includes post- S_3 phases such as chl, hb/ts, ab, ser, stp, carb, sul.

Structurally upper metapelites

Sample UM consists essentially of quartz, white mica, chloritoid porphyroblasts and garnet. It displays layers dominated by quartz and white mica respectively. Chloritoid and garnet are concentrated in the micaceous domains. The matrix foliation (S_3) is parallel to the layering and contains quartz, muscovite (type 3, 3.06–3.08 Si pfu, $X_{Na} = 0.06$), paragonite (type 3; $X_{Na} = 0.93$), chlorite (type 3; $X_{Fe} = 0.60$), garnet (0.1–0.4 mm in average, locally up to 1 mm), ilmenite (MnO = 3.11 wt%, i.e. ~9% pyrophanite) and rare elongated crystals of chloritoid (type 3; 0.5–1 mm long, $X_{Fe} = 0.81$ 0.82). It is not clear whether these chloritoid crystals really belong to the foliation or represent reoriented crystals of an older generation of chloritoid (type 2). Small crystals of tourmaline are relatively widespread in the foliation. The foliation wraps around clusters containing abundant large stubby crystals of chloritoid (type 2; up to 4 mm long, $X_{Fe} = 0.80$ 0.84), commonly lacking a preferred orientation. Garnet, white mica and minor chlorite, quartz, rutile and ilmenite are also present in these clusters. Chloritoid porphyroblasts contain numerous tiny inclusions of tourmaline, rutile, phengitic muscovite (type 2; Si = 3.33–3.34 pfu, $X_{Na} = 0.04$), paragonite (type 2; $X_{Na} = 0.95$), garnet and locally ilmenite

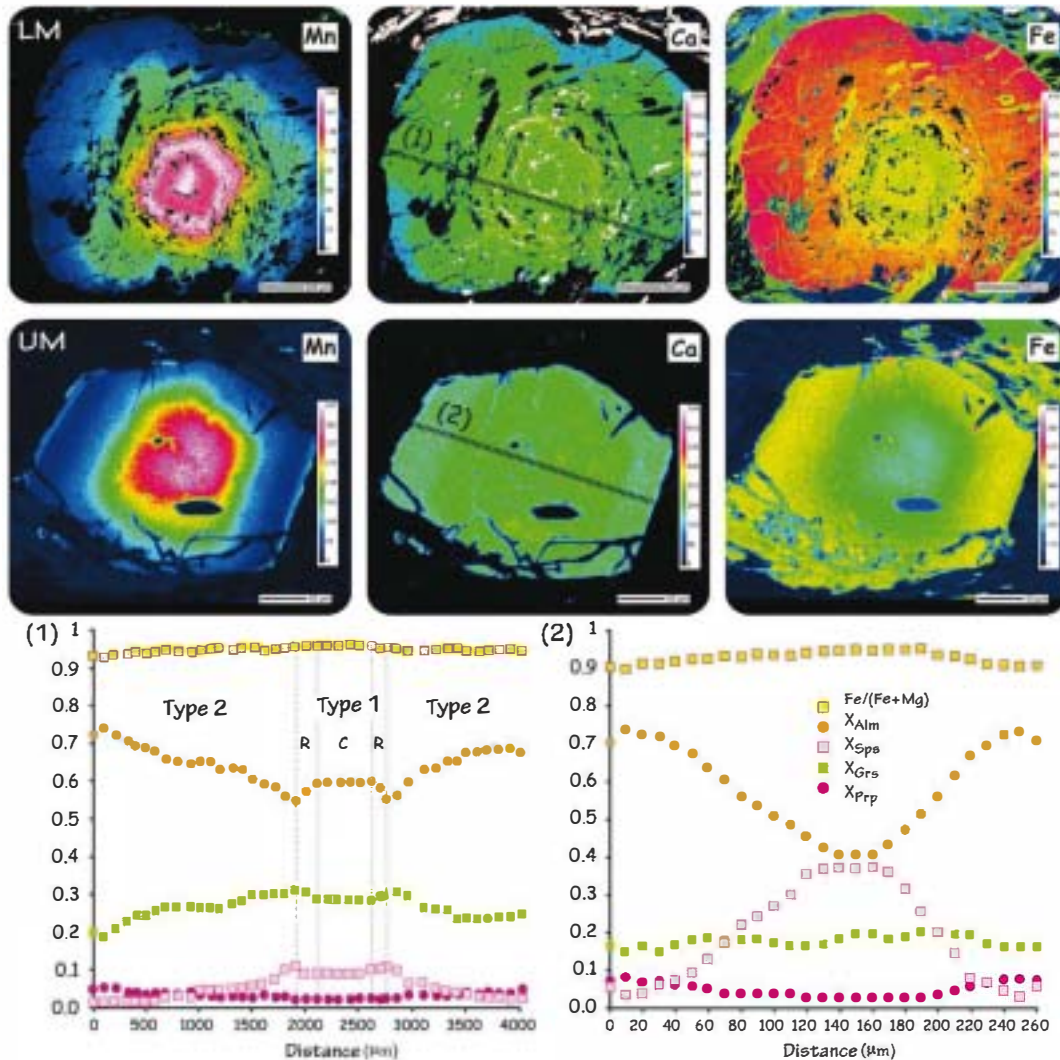


Figure 4. X-Ray maps and chemical profiles illustrating zoning of garnet porphyroblasts from the Ceán Schists. (a) Types 1 & 2 garnet from the lower metapelites (profile 1). (b) Garnet from the upper metapelites (profile 2). Thick dashed lines on the X-ray maps indicate the position of the profiles. The location of each garnet is indicated in Fig. 3.

that define an internal foliation, S_2 . Garnet inclusions are euhedral and significantly smaller (0.02–0.06 mm) than the matrix crystals (Fig. 3b). Chemical zoning of garnet (Fig. 4; profile 2) is characterized, from core to rim, by a decrease in spessartine (Sps38 → 5), balanced by an increase in almandine (Alm41 → 73) and pyrope (Prp2 → 9). X_{Fe} decreases regularly from 0.96 to 0.93. The grossular content varies irregularly between Grs20 and Grs16, with a tendency to decrease towards the rim. Finally, an increase in spessartine (Sps5 → 7) and X_{Fe} (0.90 → 0.93) is observed in the outermost rim, together with an inversion of the general zoning pattern of pyrope (Prp9 → 8) and almandine (Alm73 → 70). Garnet inclusions in chloritoid display the same type of zoning. However, the rims lack the reversal in spessartine zoning and their composition (Alm61 Prp4 Grs18 20 Sps18) suggests that they correspond to the matrix crystals, the growth of which

was arrested by the inclusion in the chloritoid (type 2). Finally, post- S_3 phases include tiny crystals of chlorite (type 3b; $X_{Fe} = 0.58$) and Fe-Ti-bearing oxides and hydroxides concentrated along the shear planes (Figs 2b & 3b).

In summary, it is inferred that the preserved mineral assemblages correspond to the sequence of two metamorphic stages, named M_2 and M_3 , according to their textural position. The M_1 event (recorded in the LM) was not identified as inclusions in garnet cores in sample UM. This event represents the early stages of subduction, and it is not possible to infer if it was not preserved in these rocks, or if they never recorded it. Evidence for M_2 is achieved by the assemblage g-ctd-mu-pa-ru ± ilm. These minerals occur preserved as inclusions in garnet and in chloritoid porphyroblasts (type 2), and define the internal fabric S_2 . M_3 corresponds to the matrix foliation S_3 and is composed of

g-chl-mu-pa-ru-ilm- \blacksquare ± ctd. The post- M_3 event includes post- S_3 phases such as chlorite and Fe/Ti-oxide.

P-T ESTIMATES

Pseudosections were calculated for the P – T domain of interest, between 350 and 600 °C and 5–25 kbar. The diagrams have been computed using THERMOCALC 3.33–3.35 (Powell & Holland, 1988) and the internally consistent thermodynamic data set 5.5 (Holland & Powell, 1998; updated Nov. 2003). References of the mixing models for solid solutions of the phases considered in the calculations are amphibole (Diener *et al.*, 2007), clinopyroxene (Green *et al.*, 2007), chloritoid (Mahar *et al.*, 1997; White *et al.*, 2000), chlorite (Le Bayon *et al.*, 2006; based on Holland *et al.*, 1998), white mica (Coggon & Holland, 2002), plagioclase (Holland & Powell, 2003), epidote (Holland & Powell, 1998), magnetite (White *et al.*, 2002), garnet, biotite, ilmenite and hematite (White *et al.*, 2005).

The rock slab of each sample used to make the thin section was crushed and analysed by XRF to obtain the bulk composition. FeO (*v.* Fe₂O₃) was analysed by wet chemical titration. Phase relations were modelled in the chemical system MnO Na₂O CaO K₂O FeO MgO Al₂O₃ SiO₂ H₂O TiO₂ Fe₂O₃ (MnNCKFMASHTO). The original compositions of the studied rocks were simplified to fit this system (Table 1). Bulk-rock compositions indicated in brackets in figure captions are those recalculated using THERMOCALC. The fluid phase was fixed as pure H₂O, initially in excess. The diagrams are shown in Figs 5 & 6. Thick lines indicate the stability field of diagnostic phases, and the thickest semitransparent lines represent the proposed P – T paths. White fields are divariant and increasing variance is shown with progressively darker shades. Mineral abbreviations are those used by THERMOCALC (see above).

Lower metapelites

A P – T pseudosection calculated in the system MnNCKFMASHTO for the analysed bulk composition with H₂O considered in excess is presented in Fig. 5a. The stability domains corresponding to the observed relicts of mineral assemblages M_1 (g, ep, sph, ru, \blacksquare) and M_2 (g, ctd, chl, gl, ru, ilm, mu, \blacksquare) are modelled in the HP and LT part of the pseudosection. However, most assemblages containing these phases are predicted to also contain lawsonite, which has not been observed either as inclusions in garnet or in the matrix. This hydrous mineral is stable over a wide P – T range in the LT blueschist facies, but rarely preserved. Pseudomorphs of this mineral can be found in the interbedded mafic rocks, so it seems possible that some of the abundant crystals of epidote present in the matrix of the schists could be the product of destabilization of lawsonite, although unquestionable pseudomorphs of this mineral were not found.

The ctd + gl paragenesis, preserved in the second generation of garnet (g₂), and characteristic of this lithology, is present in the uppermost part of the diagram between 20 and 22 kbar, and 400 and 500 °C. However, in this field, the calculated composition of garnet does not correspond to that observed in g₂. The isopleth values corresponding to type 2 garnet cores (g_{2c}) (Grs = 28–32% and Sps = 5–11%) intersect in the lower pressure chloritoid-absent field (at 18 kbar and 470 °C; see shaded star (1) in Fig. 5a). The isopleths that represent the garnet rim (g_{2r}) (Grs = 28–19% and Sps = 5–1%) intersect in the same field at higher pressures (~20 kbar and 490 °C; see shaded star (2) in Fig. 5a). Therefore, it is not possible to infer a reasonable P – T evolution for this sample because garnet zoning does not fit with the petrographic observations.

Although considering water in excess for the petrological modelling is a good approximation in most metapelites along the prograde path, crystallization of strongly hydrous minerals, like lawsonite, at high pressures and low temperatures may lead to H₂O-undersaturation as metamorphism progresses (e.g. Guiraud *et al.*, 2001; Ballèvre *et al.*, 2003; Clarke *et al.*, 2006). The available amount of H₂O also has an influence on the position of the compositional isopleths. To estimate the amount of H₂O available in the system at peak conditions, a P – X (H₂O) pseudosection has been calculated at 480 °C (Fig. 5b). The temperature corresponds to that estimated for the peak conditions from pseudosection approach (Fig. 5). However, other temperature values have been tested and the exact value does not have a significant effect on the result. The assemblage corresponding to the crystallization of the second generation of garnet (g-ctd-chl-gl-law*-ru-ilm + mu, \blacksquare) is stable between 21 and 23 kbar under H₂O-saturated conditions, but extends to slightly lower pressures (down to 20.5 kbar) with the decreasing amount of H₂O. In this four-variant field, the isopleths corresponding to the composition of the outer part of garnet 2 (g_{2r}) (Grs = 28–19%, Sps = 5–1%) intersect between X_{H_2O} of 13.75 and 15%. Therefore, the available amount of H₂O was set to 14.375 mol.% (~14.4 mol.%), corresponding to the average of these values (see shaded area in Fig. 5b). In addition, with the estimated amount of water (14.4 mol.%), a P – X (Fe₂O₃) pseudosection at 480 °C has been calculated to explore the effect of varying the Fe₂O₃ content for sample LM (Fig. 5c). According to this diagram, the isopleths of interest intersect in a wide area between the Fe₂O₃ values analysed and the double of it (see shaded area in Fig. 5c). Therefore, this diagram yields no constraints on the amount of Fe₂O₃ present in the rock, although it excludes values significantly lower than the analysed one. A new P – T pseudosection has been computed in the MnNCKFMASHTO system for the analysed bulk composition and the amount of H₂O fixed at 14.4% (Fig. 5d; Table 1b). The diagram shows that the rock

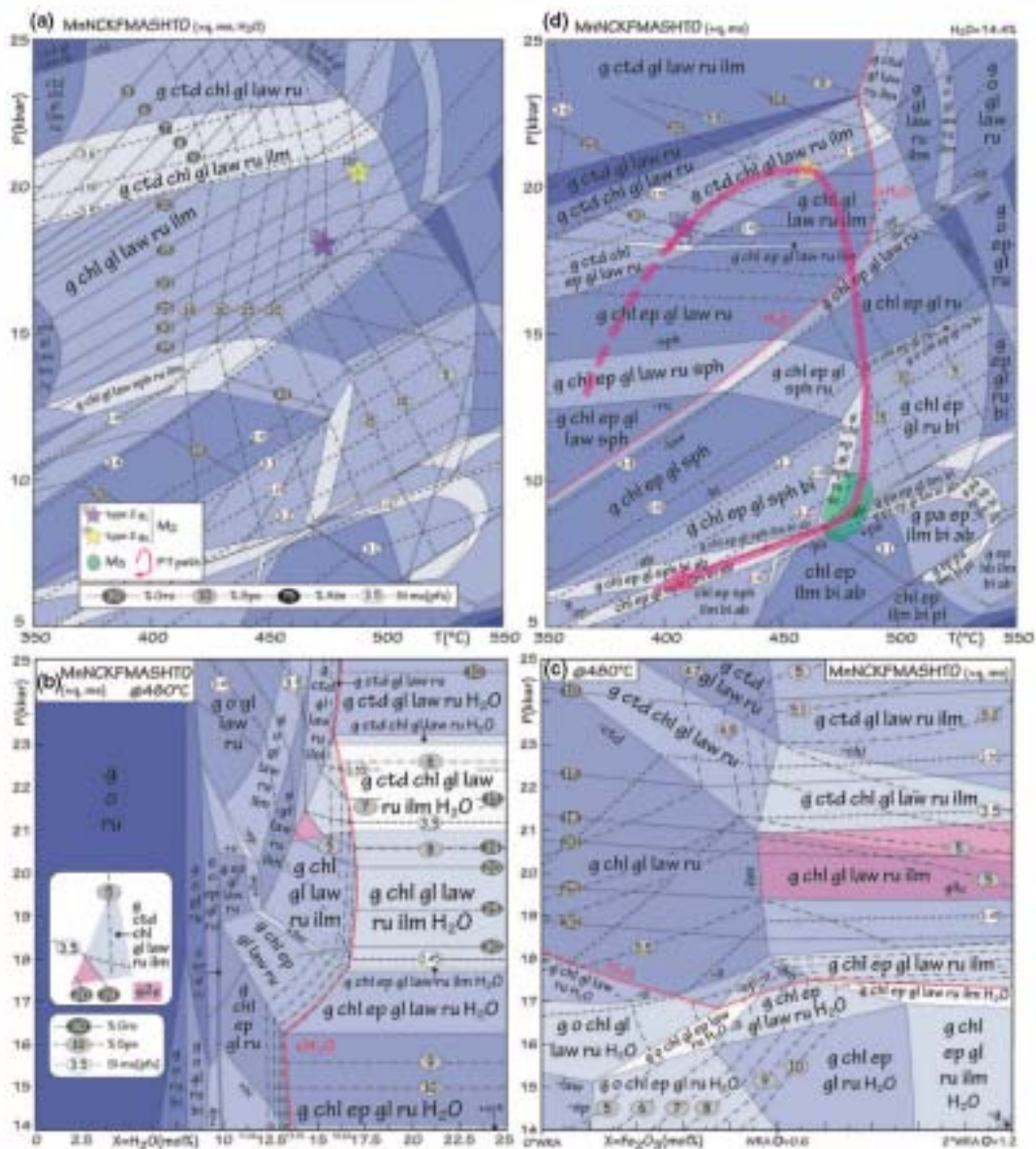


Figure 5. Sample LM [SiO₂:66.15; TiO₂:0.87; Al₂O₃:11.55; FeO:7.72; O:0.60; MnO:0.17; MgO:5.00; CaO:3.16; Na₂O:1.40; K₂O:3.37]. (a) *P*–*T* pseudosection with H₂O in excess. (b) *P*–*X*(H₂O) pseudosection calculated at 480 °C. White box in the left shows a detail of the area of interest. (c) *P*–*T* pseudosection with H₂O = 14.4%. (d) *P*–*X*(Fe₂O₃) pseudosection calculated at 480 °C with H₂O = 14.4%. WRA = original whole-rock analysis from XRF. See text and Table 1 for details.

is water saturated at LPs and HTs, but fluid absent under HP LT conditions. The HP part of the diagram (> 18 kbar) is characterized by the presence of gl + ctd and the absence of epidote (stable at < 18 kbar). Titanite is present at pressures lower than ~15 kbar and temperatures lower than 480 °C. Rutile is stable at pressures higher than ~12 kbar or temperatures in excess of 470 °C. Biotite is stable in the LP, HT part of the diagram. The stability of paragonite is modelled only at > 470 °C and < 11 kbar (Fig. 5d).

The type 1 garnet inclusions (ep, sph, ru, q) are inferred to represent relicts of the former full assemblage

g-chl*-ep-gl*-law*-ru-sph-mu*-q, suggesting that the rock passed through the corresponding stability field at 350–380 °C, 12–14 kbar. Garnet 2 cores equilibrated then in the field g-ctd-chl-gl-law*-ru-ilm + mu, q. This area is a relatively wide field at ~360–480 °C, 18–22 kbar. *P*–*T* conditions corresponding to the growth of garnet 2 have been refined based on the intersection of isopleths. The isopleths corresponding to the composition of type 2 garnet core (g_{2C}) (Sps₅₋₁₁, Grs₂₈₋₃₂) and muscovite inclusions (mu₂, Si = 3.45–3.50 pfu) intersect between ~18 and 19 kbar, and ~400 and 420 °C (shaded star (1) in Fig. 5d). Continuous decrease in grossular and spessartine

towards garnet 2 rims (g2_R) (Grs28 → 19; Sps5 → 1) suggests further heating at increasing pressure up to ~460 °C, 21 kbar (shaded star (2) in Fig. 5d). The matrix foliation (M₃) assemblage is defined by the occurrence of muscovite, paragonite, biotite, chlorite, epidote, Na Ca amphibole, ilmenite and titanite, and the absence of chloritoid. The appearance of epidote indicates < 18 kbar for the M₃ event. Biotite is stable at < 16 kbar, ilmenite and paragonite at < 11 kbar. The presence of paragonite suggests temperatures higher than 470 °C, whereas titanite is stable at < 480 °C. Although all these phases are not stable together in a single field of the pseudosection, their stability domains are extremely close in the region ~8–10 kbar, 470–490 °C, which is inferred to represent the approximate conditions of development of the main foliation S₃ (green ellipse in Fig. 5d). This point is further discussed below. In any case, this suggests significant subisothermal decompression between M₂ and M₃. Finally, the late crystallization of albite (post-M₃) indicates pressures lower than ~8 kbar and a probable further evolution towards lower P–T (Fig. 5d). Although this pseudosection accounts quite well for the petrographic evolution of sample LM in general terms, the modelled composition of amphibole along the post-M₂ path does not agree with that of the observed Na Ca amphiboles. This issue will also be discussed below.

Upper metapelites

A P–T pseudosection has been calculated in the MnNCKFMASHTO model system for the bulk composition obtained by XRF and the amount of FeO (v. Fe₂O₃) obtained by titration (Fig. 6). To check that the bulk composition does not reach H₂O-undersaturated conditions during the prograde evolution, the amount of H₂O was set so that the rock is just fluid saturated in the HP part of the field ctd-chl-pa-ep-ilm-ru + q,ms, along the LP stability limit of lawsonite. This field corresponds to a P–T domain through which the rock would pass, when following a hypothetical, but probable P–T path, before entering the stability domain of lawsonite. Indeed, as discussed above (see also Ballèvre *et al.*, 2003; Clarke *et al.*, 2006), the formation of lawsonite commonly leads to H₂O undersaturation. However, in this low-Ca metapelite, the modelled modal amount of lawsonite is very low. As a result, using this approach, the assemblages are H₂O undersaturated at low pressures and temperatures, with a aqueous fluid stabilized at higher conditions (Fig. 6b). Consequently, the entire prograde evolution of this rock occurs under H₂O-saturated conditions and water is considered in excess in the following calculations.

In this P–T pseudosection (Fig. 6a), garnet is stable at > 500 °C, epidote is stable at < 520 °C and < 18 kbar and glaucophane is predicted to be stable from 15 to 21 kbar, at < 590 °C. Epidote and glaucophane have not been found either as inclusions or in

the matrix. Therefore, based on the petrographic observations the four-variant field g-ctd-chl-pa-ilm-ru + q,ms located between 12 and 15 kbar and at > 510 °C reflects the paragenesis corresponding to the matrix foliation. However, this pseudosection cannot be used to infer the equilibration conditions of the garnet core, as the observed amount of spessartine in the garnet core (Sps38–40; Fig. 4b) is not modelled anywhere in the diagram. The maximum values predicted in the diagram are Sps15. One reason may be the relatively high amount of Fe₂O₃ analysed in this sample, uncommon in typical pelites. Although sample UM does not appear to be altered in hand specimen or in thin section, the concentration of Fe-bearing oxides/hydroxides along shear planes (Fig. 3b) suggests that the Fe₂O₃ proportion in the original rock may have been significantly lower compared with the result of the analysed bulk composition, possibly due to the circulation of oxidizing fluids. A series of pseudosections was recalculated with progressively lower amounts of Fe₂O₃ ('O' in the bulk composition), with significant changes only being observed when the amount of Fe₂O₃ was close to zero. The highest values predicted in the diagram for the spessartine and grossular isopleths calculated for the garnet core composition intersect at ~16 kbar in the three-variant field g-ctd-pa-ep-gl-ilm-ru + q,ms (shaded star in Fig. 6a). Therefore, this domain seemed the most suitable for obtaining spessartine values closer to the observed ones by modifying the amount of Fe₂O₃ in the bulk composition. Trying to estimate a reliable amount of Fe₂O₃ for this sample, a T–X(Fe₂O₃) pseudosection was calculated at 16 kbar (Fig. 6c). This diagram shows that the isopleths corresponding to the composition of the garnet core intersect between 425 and 440 °C in the four-variant field g-ctd-chl-pa-gl-law-ru + q,ms for Fe₂O₃ = 0.05 (shaded star in Fig. 6c). Consequently, a P–T pseudosection has been recalculated with this value, O = 0.05 (Fig. 6d; Table 1b).

Compared with the original diagram, in this P–T pseudosection, garnet stability increases notably towards lower temperatures (from 510 to 420 °C) and glaucophane is stable at pressures higher than 11 kbar. The syn-S₃ matrix assemblage, g-ctd-chl-pa-ilm-ru + mu, q is modelled in the relatively LP and HT part of the diagram. The analysed composition of muscovite (Si < 3.1 pfu) is compatible with the equilibration of the matrix in the LP part (< 11 kbar) of this field. The isopleths corresponding to the proportions of grossular and spessartine in the garnet cores (18–20 and 38–40% respectively) intersect in the four-variant field g-ctd-chl-pa-gl-law-ru + q,ms at ~15–16 kbar, 430 °C (shaded star (1) in Fig. 6d). One of the principal characteristics of the garnet zoning observed in the sample is a continuous decrease of spessartine, whereas the grossular content remains at an approximately stable value. This evolution may only be explained if a Ca-rich phase like epidote or lawsonite coexists with garnet (shaded star (2) in Fig. 6d). Beyond, both

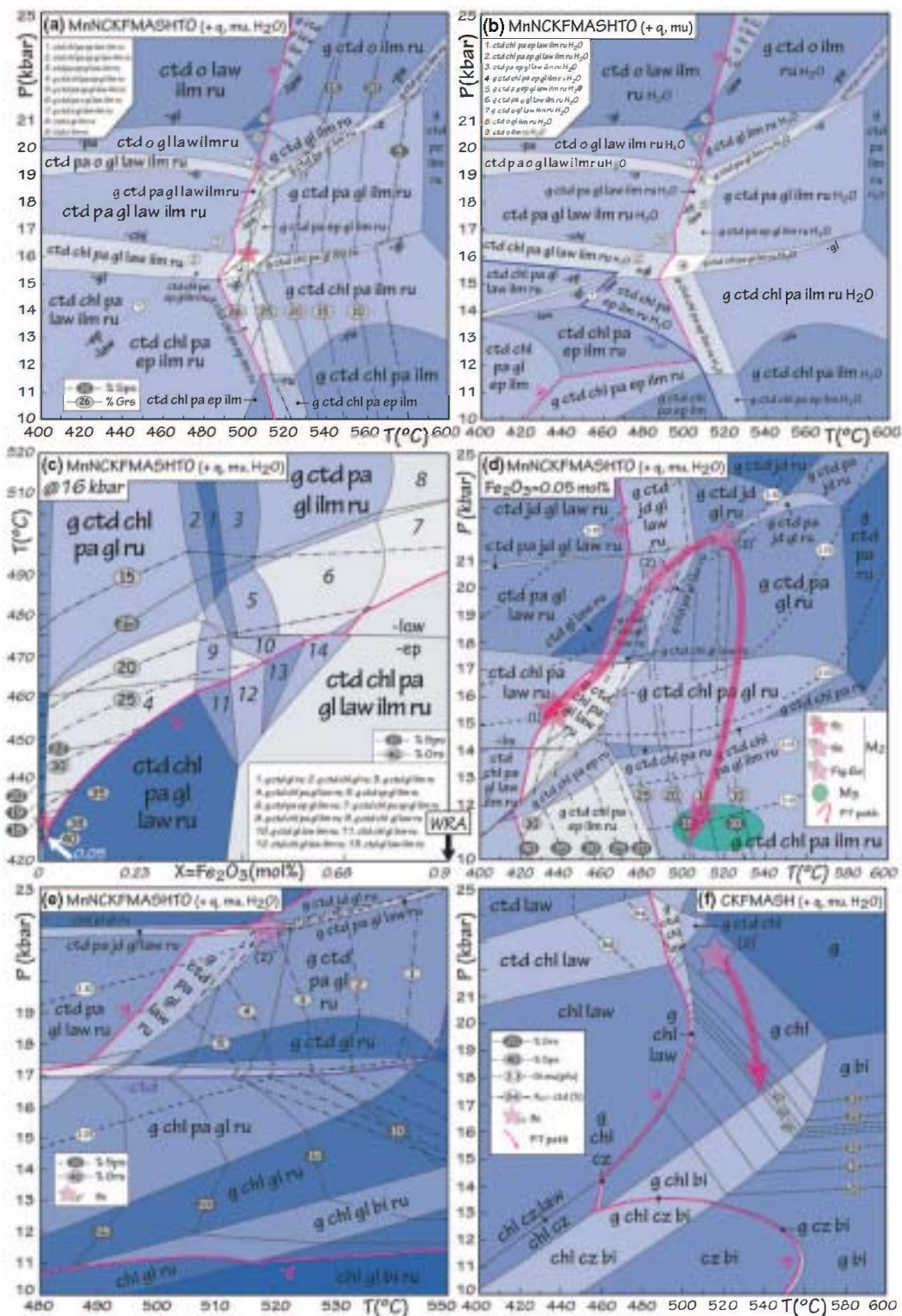


Figure 6. Sample UM [SiO₂:68.63; TiO₂:0.66; Al₂O₃:14.70; FeO: 7.68; O:0.89; MnO:0.26; MgO:3.05; CaO:0.24; Na₂O:0.98; K₂O:2.91] (a) *P* *T* pseudosection with H₂O in excess. (b) *P* *T* pseudosection calculated for the analysed bulk-rock composition showing dehydration along the stability limit of lawsonite. (c) *T* *X*(Fe₂O₃) pseudosection calculated at 16 kbar between 420 and 520 °C; WRA original whole-rock analysis from XRF. (d) *P* *T* pseudosection with Fe₂O₃ = 0.05 mol%. The star (2)* is inferred from Fig. 6e. (e) *P* *T* pseudosection calculated for the bulk-rock composition after fractionation of garnet and chloritoid. (f) *P* *T* pseudosection calculated in the CKFMASH system for the bulk-rock composition after fractionation. The star (2)* is inferred from (e). See text and Table 1 for details.

isopleths become nearly parallel and a decrease in spessartine is accompanied by a decrease in grossular, which is not observed in the sample. However, at the lawsonite-out line of the field $g\text{-ctd-pa-gl-law-ru} + \mu$, for grossular contents between 15 and 20%, corresponding to those observed in the sample, the spessartine content is $\sim 15\%$, whereas the value observed in the garnet rim is $\sim 3\%$ (Fig. 4b).

As Mn is mostly stored in garnet cores during prograde metamorphism, this inconsistency could be related to the fractionation of whole-rock composition due to the garnet growth. However, progressive removal of even all crystallizing garnet from the bulk composition does not reproduce the observed garnet rim compositions. Although much poorer in Mn than garnet, chloritoid does contain Mn and is present in significant quantities in the sample (and the model pseudosection). Furthermore, clusters of large chloritoid crystals in the sample appear shielded from the deformation associated with the development of the main foliation and could be effectively inert during the recrystallization of the rock matrix (and the crystallization of the rims of matrix garnet). Progressive fractionation of garnet and the removal of 95% of chloritoid at the point when the modelled crystallizing garnet has the composition of the rims of the garnet inclusions in chloritoid results in a Mn-poor bulk composition (Table 1b) and a corresponding P T pseudosection depicted in Fig. 6e. This model reproduces the observed garnet zoning, with the garnet rims crystallizing at the lawsonite-out limit of the field $g\text{-ctd-pa-gl-law-ru} + \mu$ at ~ 21.5 kbar, 510–520 °C.

The composition of muscovite (Si ~ 3.3 pfu) modelled along the path inferred for the garnet growth is compatible with the values observed in the muscovite inclusions in the chloritoid porphyroblasts. Consequently, the preserved garnet zoning constrains the prograde P T evolution of the sample from ~ 16 kbar and 430 °C to ~ 21 kbar and 510 °C.

The lack of further garnet growth suggests that the subsequent evolution must have occurred at constant or decreasing garnet mode. Indeed, partial garnet resorption is suggested by the local increase of spessartine at the very rim of the matrix crystals (Fig. 4). The isopleths of garnet mode (not represented) are essentially parallel to the isopleths of the spessartine content. Their position suggests an evolution dominated by decompression at approximately constant or decreasing temperature. Nevertheless, in Fig. 6e, such an evolution systematically passes through fields containing glaucophane, which is not present in sample UM. Glaucophane disappears from the model mineral assemblages at pressures lower than 8 kbar (not represented). But, all fields at pressures lower than 10–13 kbar contain biotite, which is not present in the sample either (Fig. 6e). However, it cannot actually be excluded that the rock passed although biotite-bearing fields because during cooling rocks become dry and diffusion inefficient (e.g. Guiraud *et al.*, 2001). Consequently, it is not

possible to interpret the formation of the matrix assemblage using this pseudosection.

Trying to overcome these problems, the chemical system was simplified to CKFMASH using the following assumptions based on the petrographic observations. Sodium was removed from the bulk composition in the form of paragonite (which is the only Na-bearing mineral in the matrix), MnO was subtracted in the form of ilmenite containing 10% pyrophanite and the remaining TiO₂ was removed as 40% rutile and 60% ilmenite (according to the modal proportions observed in thin section). These minerals are therefore considered *de facto* in excess. The resulting P T pseudosection (Fig. 6f) has chloritoid in the HP LT corner of the diagram, whereas biotite is stable in the LP HT part. The stability field that approaches best the observed matrix assemblage is $g\text{-chl} (+\mu + \text{pa-ilm-ru})$, stable at temperatures between 460 and 560 °C and $13 < P < 23$ kbar. The P T conditions of the formation of the matrix remain therefore largely unconstrained.

DISCUSSION

The two samples representative, respectively, of the lower and upper level of the Ceán Schists in the Upper Sheet of the MTU have recorded similar P T evolutions characterized by a prograde P T path in blueschist facies conditions, peaking at 21–22 kbar. The temperatures recorded in the UM are slightly higher than those from the LM (Fig. 7a). Both samples could have experienced a slightly different evolution due to their different position in the orogenic wedge (Fig. 7b). In the LM, the blueschist facies assemblages were overprinted by the regional foliation developed at significantly lower pressures (8–10 kbar, 470–490 °C). Whereas the calculated phase diagrams and the proposed metamorphic evolution account reasonably well for the first-order petrographic observations, and are in agreement with the mineral chemistry in both the LM and the UM, several details need to be discussed.

Phase diagrams

For both rock types, the first step was to calculate a P T pseudosection using the water-saturated analysed bulk composition. Confronted with the lack of compatibility between the observations and the modelling results, various compositional parameters that may significantly modify the appearance of the pseudosection have been investigated (calculating parts of P T or P/T X pseudosections), to obtain coherent results. For the LM, the H₂O content appeared to be the critical factor. Fe³⁺ appeared to play the major role for UM, whereas the low mode of lawsonite in this low-Ca pelite did not lead to H₂O-depletion and the rock remained H₂O saturated during the prograde evolution.

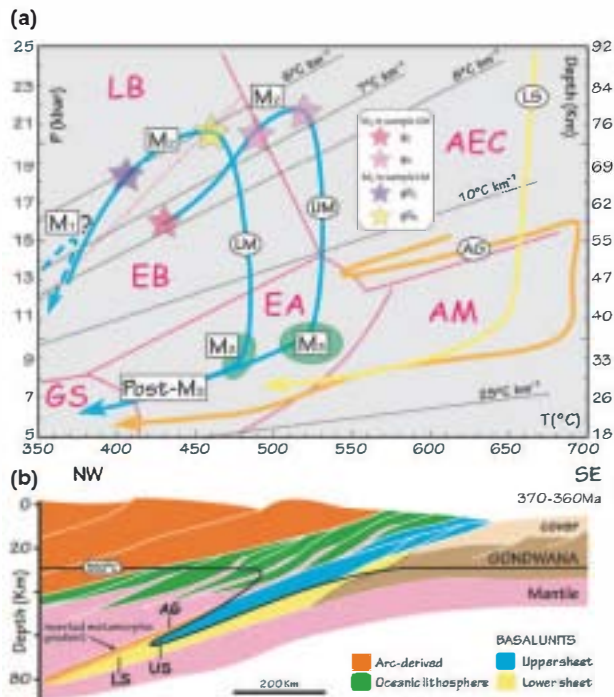


Figure 7. (a) P – T diagram showing the metamorphic paths of the Ceán Schists (LM and UM). The P – T paths for the Lower Sheet of the Malpica Tui Unit (unpublished data) and for the Agualada Unit (Arenas *et al.*, 1997) are also included. Metamorphic facies field abbreviations: GS, greenschist facies; EA, epidote amphibolite facies; AM, amphibolite facies; LB, lawsonite blueschist facies; EB, epidote blueschist facies and AEC, amphibole eclogite facies (Evans, 1990 (dashed line); Maruyama *et al.*, 1996). (b) Schematic cross-section of the subduction zone operating in the NW Iberian Massif at 370–360 Ma. US, upper sheet; LS, lower sheet; AG, Agualada Unit. Based on Martínez Catalán *et al.* (1996).

In both samples, the modelling accounts quite well for the observed paragenetic sequence. It can be objected that all the phases inferred to be stable during the prograde part of the P – T evolution, in particular lawsonite and glaucophane, are not observed in the thin sections (with the exception of the M_2 glaucophane inclusion in garnet of the LM). However, inclusions typically only represent remnants of the initial full assemblages. In more detail, in the LM, the absence of lawsonite has already been discussed above and can be explained by the classic replacement by epidote during decompression. In the UM, the modelled proportion of both lawsonite and glaucophane is very low (max. 0.9 and 3.5% respectively) making their preservation improbable.

In the LM, no stability field can account for the presence of all the M_3 minerals in the S_3 foliation. The stability domains of the M_3 minerals, in particular paragonite, chlorite and titanite are extremely close to one another in the topologically complex region at around 8 kbar, 470 °C, but do not overlap. Nevertheless, it can be argued that along a P – T path crossing

this region, a rock could develop these minerals sequentially, giving the impression of an equilibrium assemblage. Alternatively, minor changes in the parameters of the mixing models for solid solutions could change the topology sufficiently to obtain the observed assemblage in one field in this P – T domain.

Similarly, only small and scattered crystals of chemically heterogeneous Na–Ca amphibole are observed in the matrix foliation. However, the amphibole predicted in the pseudosection has systematically a high-glaucophane content and is relatively abundant (18–14 mol.%) down to pressures of ~8 kbar, when albite becomes stable. When reaching the field g - chl - ep - gl - sph - bi - ab + q , ms at 7 kbar, an abrupt decrease in the mode of amphibole (from 14 to 3 mol.%) coincides with an increase of the proportion of hornblende. This increase is compatible with the presence of Ca-amphiboles, such as hornblende and tschermakite, observed in the post- S_3 textural position. Although the amphibole chemical composition along the proposed P – T path never coincides with the analysed compositions, this qualitative evolution is compatible with the crystallization of the post- S_3 phases under relatively LP conditions, of the order of 7–8 kbar, < 480 °C.

In sample UM, it is difficult to estimate reliably the equilibration conditions of the matrix foliation (S_3). In the P – T pseudosection calculated for the analysed bulk composition (Fig. 6a, b), the syn- S_3 matrix assemblage, g - ctd - chl - pa - ilm - ru + q , ms and the composition of the matrix muscovite ($Si < 3.1$ pfu) suggest equilibration of the matrix in the LP and HT part of the diagram (< 11 kbar, > 480 °C). However, this diagram does not account for the observed garnet zoning. This can only be explained if significant fractionation of garnet and chloritoid takes place (Fig. 6e). Then, however, any reasonable P – T evolution systematically passes through fields containing glaucophane, which is not present in the sample, unless paragonite is forced in excess in a model system reduced effectively to CKF-MASH (Fig. 6f).

The first reason for this can be a problem with the solid-solution models. Unfortunately, even using the most recent glaucophane (Diener & Powell, 2012) and white mica (Smye *et al.*, 2010) models only results in minor differences in the pseudosection and does not solve the problem. It appears that glaucophane is ‘too stable’, in particular with respect to paragonite. A second reason may be related to problems with the identification of the effective bulk composition. This can be related to the deformation-enhanced fractionation of the bulk composition in a layered rock. In certain layers, the initial bulk composition undergoes fractionation during the growth of garnet and chloritoid porphyroblasts. During the subsequent deformation, a certain proportion of these porphyroblasts is preserved in undeformed domains, forming the observed chloritoid + garnet-rich clusters (Fig. 3b). Other layers and a part of the garnet-chloritoid clusters recrystallize during the formation of the S_3 foliation.

For these domains, the unfractionated composition and hence the original pseudosection (Fig. 6a,b) is still applicable. Alternatively, problems may also be related to the presence in the sample of some minerals that should have been removed from the effective bulk composition, like tourmaline. However, the crystallization of such minerals is generally related to fluid circulation, which may occur at different stages of the metamorphic evolution, resulting in the modification of the bulk composition at a point that may be difficult to estimate. Finally, a major change in the oxidation conditions during the evolution of the rock cannot be excluded, with important consequences on the stable mineral assemblages, as discussed before.

Fluid-absent prograde metamorphism

The possibility of reduced water availability in certain geodynamic scenarios allows rocks to experience a fluid-absent prograde evolution during subduction. A vast majority of metamorphic reactions have a dehydration character and produce H₂O fluid when crossed upon heating, during the prograde evolution. Accordingly, most rocks are saturated in H₂O, which is then commonly considered in excess for petrological modelling. Whereas this approach yields correct results in most cases, several exceptions merit highlighting: polycyclic evolution, partial melting, retrograde evolution and subduction metamorphism. The latter is the one that concerns this study. Metamorphism in subduction zones is characterized by low geothermal gradients (steep in a *P-T* diagram). Rocks following these gradients may cross some dehydration reactions in the 'wrong', H₂O-consuming direction. This is the case of the reactions involving lawsonite, which have a relatively 'flat' slope with lawsonite being stable at the HP, LT side. Consequently, rocks become H₂O undersaturated with important implications for the phase relations and mineral assemblages encountered in such environments (e.g. Ballèvre *et al.*, 2003; Clarke *et al.*, 2006). Unlike their metabasic counterparts, pelitic rocks are depleted in Ca and can only form limited quantities of lawsonite. It is then not common for a metapelite to experience a fluid-absent prograde metamorphism, which can be expected in metabasic rocks. Sample LM, with a composition intermediate between a pelitic and a basic one, is more likely to have undergone a fluid-absent prograde metamorphism than a pure pelite. On the contrary, sample UM, with a true pelitic composition, experienced a fluid-bearing prograde metamorphism.

Tectonic implications inferred from garnet zoning

The zoning of type 1 garnet in sample LM is not accounted for satisfactorily by the phase diagrams, as the predicted garnet composition does not match the observed one in the appropriate assemblage fields. This may have several reasons including problems with

activity composition relations in Mn-bearing systems, inappropriate estimation of the effective bulk composition or the oxidation state of the rock, or problems with the degree of H₂O (under)saturation of the mineral assemblages. However, the preserved zoning can be used to draw some qualitative inferences about the evolution of the rock. Whereas the core of garnet 1 displays a decrease in spessartine (Sps18 → 09), the rim displays a reverse trend (Sps9 → 11) to reach values characteristic of the core of garnet 2 (Sps11) (Fig. 4). Because of the strong fractionation of Mn into garnet, garnet growth is systematically associated with the decrease in the proportion of spessartine. Similarly, an increase of spessartine is typically related to a decrease in pressure and/or temperature (cf. Fig. 5). Consequently, the decrease of spessartine in the garnet 1 core can be interpreted in terms of a prograde growth. Higher spessartine content preserved in the core of garnet 2 suggests that it began to crystallize at *P-T* conditions lower than those reached by the rim of garnet 1. This suggests a slightly more complex metamorphic evolution characterized by a stage of partial exhumation during the subduction process (Fig. 7a). The reverse zoning in the garnet 1 rim may be related either to partial resorption or to a diffusional reequilibration with the garnet 2 core (e.g. Banno & Chii, 1978; Tracy, 1982). Moreover, type 1 garnet contains the earliest foliation (S₁) preserved in the Ceán Schists, which is not observed in samples from the higher structural levels. Therefore, the M₁ event was recorded at least by the LM and the first subduction-related stage is only preserved in the lower structural levels of the series (Fig. 7a).

Implications for the Variscan subduction in NW Iberia

The *P-T* results obtained from pseudosection calculations yield first-order constraints for geodynamic models: the maximum depth reached by the Upper Sheet of the MTU during subduction and the geothermal gradient. *P-T* conditions of 21–22 kbar and 460 and 520 °C in the lower and UM, respectively, correspond to an approximate depth of ~76–80 km and a geothermal gradient of 6–7 °C km⁻¹, typical of relatively cold subduction zones (Fig. 7a). The relative present-day tectonostratigraphic position of the MTU (blueschist facies Upper Sheet and eclogite facies Lower Sheet) and the Basal Units of the neighbouring Ordenes Complex (Aigualada Unit in Fig. 1) suggests that the original position of the different units during subduction was preserved despite the subsequent post-HP history (see e.g. Martínez Catalán *et al.*, 1996). The important relative movements between the Upper and the Lower Sheet, reflected by their tectonic extensional contact, produced the superposition of sheets located at different depths in the subduction complex, but their relative position in the subducting slab was probably not altered. The differences in the *P-T* paths (Fig. 7a) between the MTU and the Aigualada Unit can be

explained on a schematic cross-section of the subduction zone at the moment when peak pressures were reached (Fig. 7b). The blueschist sheet of this study (Ceán Schists) is sandwiched between two eclogitic units: the Lower Sheet of MTU below and the Aguada Unit above. The highest temperatures during subduction are found in Aguada, where the temperature peak is ~ 720 °C and pressure is > 14 kbar (Arenas *et al.*, 1997). The fact that highest temperatures have been recorded on the top of the subducting slab demonstrates the existence of an inverted metamorphic gradient at the top of the subducting slab. The presence of a blueschist sheet sandwiched between two eclogite facies sheets is interpreted as a consequence of the geometry of the isotherms (Fig. 7b).

CONCLUSIONS

From this study we can conclude that:

- 1 The Upper Sheet of the MTU recorded a three-stage metamorphic evolution involving (i) Early subduction-related medium-pressure/LT metamorphism (M_1) roughly constrained at ~ 350 – 380 °C, 12–14 kbar, which is only preserved in the basal part (LM) of the Ceán Schists. (ii) Subduction-related blueschist facies prograde metamorphism (M_2) going from ~ 19 kbar, 400 °C to 21 kbar, 460 °C in the structurally LM, and from 16 kbar 430 °C to 21–22 kbar, 520 °C in the UM. (iii) Exhumation-related metamorphism (M_3) is characterized by a decompression to 8–10 kbar, ~ 470 – 490 °C in the LM. This decompression is also recorded in the UM, but it was not possible to estimate precise P – T conditions.
- 2 The pseudosection calculations indicate that the prograde evolution in subduction zones may occur in H_2O -undersaturated conditions due to the crystallization of lawsonite, even in metapelitic rocks. This significantly influences phase equilibria and hence the P – T estimates.
- 3 The proportion of ferric iron has a strong influence on the phase equilibria of HP metapelites. However, the analysed values of Fe_2O_3 may not reflect the oxidation state during the main metamorphic evolution and are probably easily modified by superficial alteration even in apparently fresh samples. The use of P/T $X(Fe_2O_3)$ pseudosections together with petrographic observations is then necessary to estimate the real oxidation state of the rocks and correctly evaluate the P – T conditions.
- 4 The Basal Units of the NW Iberian Massif formed part of a slab subducted beneath Laurussia at the onset of the Variscan collision. The units are separated and displaced by tectonic contacts. However, the succession of the P – T conditions recorded by the different basal units preserves the original thermal structure of the subduction zone in the northern margin of Gondwana.

ACKNOWLEDGEMENTS

This work was financially supported by the Spanish Project CGL2007-65338-CO2-01 (Ministerio de Ciencia e Innovación). We thank A. Fernández Larios and J. González del Tanago from the Spanish National Electronic Microscopy Centre (ICTS/CNME-UCM), and P. Lozano from the UCM, for their technical support. We are grateful to M. Ballèvre for stimulating discussions. This manuscript was significantly improved by the careful and constructive reviews from F. Korhonen and an anonymous referee. Editorial handling by R. Powell is gratefully appreciated.

REFERENCES

- Abati, J., Gerdes, A., Fernández Suárez, J. *et al.*, 2010. Magmatism and early Variscan continental subduction in the northern Gondwana margin recorded in zircons from the Basal Units of Galicia, NW Spain. *Geological Society of America Bulletin*, **122**, 219–235.
- Arenas, R., Rubio Pascual, F.J., Diaz Garcia, F. & Martínez Catalan, J.R., 1995. High-pressure micro inclusions and development of an inverted metamorphic gradient in the Santiago Schists (Ordnes Complex, NW Iberian Massif, Spain): evidence of subduction and syncollisional decompression. *Journal of Metamorphic Geology*, **13**, 141–164.
- Arenas, R., Abati, J., Catalan, J.R.M., Garcia, F.D. & Pascual, F.J.R., 1997. P – T evolution of eclogites from the Aguada Unit (Ordnes Complex, northwest Iberian Massif, Spain): implications for crustal subduction. *Lithos*, **40**, 221–242.
- Atherton, M.P. & Brotherton, M.S., 1982. Major element composition of the pelites of the Scottish Dalradian. *Geological Journal*, **17**, 185–221.
- Ballèvre, M., Pitra, P. & Bohn, M., 2003. Lawsonite growth in the epidote blueschists from the Ile de Groix (Armorican Massif, France): a potential geobarometer. *Journal of Metamorphic Geology*, **21**, 723–735.
- Banno, S. & Chii, S., 1978. A model to explain the Mn enrichment in the rim of zoned garnet. *Geochemical Journal*, **12**, 253–257.
- Bosse, V., Ballèvre, M. & Vidal, O., 2002. Ductile thrusting recorded by the garnet isograd from blueschist-facies metapelites of the Ile de Groix, Armorican Massif, France. *Journal of Petrology*, **12**, 485–510.
- Chopin, C., 1981. Talc Phengite: a widespread assemblage in high-grade pelitic Blueschists of the Western Alps. *Journal of Petrology*, **22**, 628–650.
- Clarke, G.L., Powell, R. & Fitzherbert, J.A., 2006. The lawsonite paradox: a comparison of field evidence and mineral equilibria modelling. *Journal of Metamorphic Geology*, **24**, 715–725.
- Coggon, R. & Holland, T.J.B., 2002. Mixing properties of phengitic micas and revised garnet phengite thermobarometers. *Journal of Metamorphic Geology*, **20**, 683–696.
- Diener, J.F.A. & Powell, R., 2012. Revised activity composition models for clinopyroxene and amphibole. *Journal of Metamorphic Geology*, **30**, 131–142.
- Diener, J.F.A., Powell, R., White, R.W. & Holland, T.J.B., 2007. A new thermodynamic model for clino- and orthoamphiboles in the system Na_2O – CaO – FeO – MgO – Al_2O_3 – SiO_2 – H_2O . *Journal of Metamorphic Geology*, **25**, 631–656.
- Díez Fernández, R., Martínez Catalán, J.R., Arenas Martín, R. & Abati Gómez, J., 2011. Tectonic evolution of a continental subduction exhumation channel: variscan structure of the basal allochthonous units in NW Spain. *Tectonics*, **30**, TC3009.

- Diez Fernández, R., 2011. *Evolución estructural y cinemática de una corteza continental subducida: la Unidad de Malpica Tui (NO del Macizo Ibérico)*. Nova Terra, A Coruña.
- Diez Fernández, R. & Martínez Catalán, J.R., 2009. 3D Analysis of an Ordovician igneous ensemble: a complex magmatic structure hidden in a polydeformed allochthonous Variscan unit. *Journal of Structural Geology*, **31**, 222–236.
- Diez Fernández, R., Martínez-Catalán, J.R., Arenas, R. & Abati, J., 2012. The onset of the assembly of Pangaea in NW Iberia: constraints on the kinematics of continental subduction. *Gondwana Research*, **22**, 20–25.
- El-Shazly, A.K. & Liou, J.G., 1991. Glaucophane chloritoid bearing assemblages from NE Oman: petrologic significance and a petrogenetic grid for high P metapelites. *Contributions to Mineralogy and Petrology*, **107**, 180–201.
- Ernst, W., 1971. Metamorphic zonation on presumably subducted lithospheric plates from Japan, California and the Alps. *Contributions to Mineralogy and Petrology*, **34**, 43–59.
- Ernst, W.G., 1973. Blueschists metamorphism and *P-T* Regimes in active subduction zones. *Tectonophysics*, **17**, 255–272.
- Ernst, W.G., 2001. Subduction, ultrahigh-pressure metamorphism, and regurgitation of buoyant crustal slices implications for arcs and continental growth. *Physics of the Earth and Planetary Interiors*, **127**, 253–275.
- Evans, B.W., 1990. Phase relations of epidote blueschists. *Lithos*, **25**, 3–23.
- Green, E., Holland, T. & Powell, R., 2007. An order disorder model for omphacitic pyroxenes in the system jadeite-diopside-hedenbergite-acmite, with applications to eclogitic rocks. *American Mineralogist*, **92**, 1181–1189.
- Guiraud, M., Powell, R. & Rebay, G., 2001. H₂O in metamorphism and unexpected behaviour in the preservation of metamorphic mineral assemblages. *Journal of Metamorphic Geology*, **19**, 445–454.
- Holland, T.J.B. & Blundy, J.D., 1994. Non-ideal interactions in calcic amphiboles and their bearing on amphibole-plagioclase thermometry. *Contributions to Mineralogy and Petrology*, **116**, 433–447.
- Holland, T.J.B. & Powell, R., 1998. An internally consistent thermodynamic data set for phases of petrological interest. *Journal of Metamorphic Geology*, **16**, 309–343.
- Holland, T., Baker, J. & Powell, R., 1998. Mixing properties and activity composition and relationships of chlorites in the system MgO-FeO-Al₂O₃-SiO₂-H₂O. *European Journal of Mineralogy*, **10**, 395–406.
- Holland, T. J. B. & Powell, R., 2003. Activity-composition relations for phases in petrological calculations: an asymmetric multicomponent formulation. *Contributions to Mineralogy and Petrology*, **145**, 492–501.
- Katagas, C., 1980. Ferroglaucofane and chloritoid bearing metapelites from the phyllite series, southern Peloponnes, Greece. *Mineralogical Magazine*, **43**, 975–978.
- Kiénaest, J.R. & Triboulet, C., 1972. Le chloritoïde dans les paragenèses à glaucophane, albite ou paragonite. *Bulletin de la Société Française Minéralogie et de Cristallographie*, **95**, 565–573.
- Korhonen, F.J., Powell, R. & Stout, J.H., 2012. Stability of sapphirine + quartz in the oxidized rocks of the Wilson Lake terrane, Labrador: calculated equilibria in NCKFMASHTO. *Journal of Metamorphic Geology*, **30**, 21–36.
- Le Bayon, B., Pitra, P., Ballèvre, M. & Bohn, M., 2006. Reconstructing *P-T* paths during continental collision using multi stage garnet (Gran Paradiso nappe, Western Alps). *Journal of Metamorphic Geology*, **24**, 477–496.
- López-Carmona, A., Abati, J. & Reche, J., 2007. Metamorphic evolution of the HP/LT Ceán Schists (Malpica Tui Unit, NW Iberian Massif). *Geogaceta*, **43**, 3–6.
- López-Carmona, A., Abati, J. & Reche, J., 2010. Petrologic modelling of chloritoid glaucophane schists from the NW Iberian Massif. *Gondwana Research*, **17**, 377–391.
- Mahar, E.M., Baker, J.M., Powell, R., Holland, T.J.B. & Howell, N., 1997. The effect of Mn on mineral stability in metapelites. *Journal of Metamorphic Geology*, **15**, 223–238.
- Martínez Catalán, J.R., Arenas, R., Díaz García, F., Rubio Pascual, F.J., Abati, J. & Marquínez, J., 1996. Variscan exhumation of a subducted Paleozoic continental margin: the Basal Units of the Ordenes Complex, Galicia, NW Spain. *Tectonics*, **15**, 106–121.
- Martínez Catalán, J.R., Arenas, R., Díaz García, F. & Abati, J., 1997. Variscan accretionary complex of northwest Iberia: terrane correlation and succession of tectonothermal events. *Geology*, **27**, 1103–1106.
- Martínez Catalán, J.R., Arenas, R., Abati, J. et al., 2009. A rootless suture and the loss of the roots of a mountain chain: the Variscan belt of NW Iberia. *Comptes Rendus Geosciences*, **341**, 114–126.
- Maruyama, S., Liou, G. & Terabayashi, M., 1996. Blueschists and eclogites of the world. *International Geology Review*, **38**, 485–594.
- Miyashiro, A., 1961. Evolution of metamorphic belts. *Journal of Petrology*, **2**, 277–311.
- Platt, J.P., 1993. Exhumation of high-pressure rocks: a review of concepts and processes. *Terra Nova*, **5**, 119–133.
- Powell, R. & Holland, T.J.B., 1988. An internally consistent dataset with uncertainties and correlations: 3. Applications to geobarometry, worked examples and a computer program. *Journal of Metamorphic Geology*, **6**, 173–204.
- Powell, R. & Holland, T.J.B., 2002. Course Notes for THERMOCALC Workshop 2002: Calculating Metamorphic Phase Equilibria (Barcelona). CD-ROM.
- Rodríguez Aller, J., 2005. *Recristalización y deformación de litologías supracorticales sometidas a metamorfismo de alta presión (Complejo de Malpica Tui, NO del Macizo Ibérico)*. O Castro, A Coruña.
- Rodríguez Aller, J., Cosca, M.A., Gil Ibarguchi, J.I. & Dallmeyer, R.D., 2003. Strain partitioning and preservation of ⁴⁰Ar/³⁹Ar ages during Variscan exhumation of a subducted crust (Malpica Tui complex, NW Spain). *Lithos*, **70**, 111–139.
- Rubio Pascual, F.J., Arenas, R., Díaz García, F., Martínez Catalán, J.R. & Abati, J., 2002. Eclogites and eclogite amphibolites from the Santiago Unit (Ordenes Complex, NW Iberian Massif, Spain): a case study of contrasting high-pressure metabasites in a context of crustal subduction. In: *Variscan Appalachian Dynamics: the Building of the Late Paleozoic Basement* (eds Martínez Catalán, J.R., Hatcher, R.D., Arenas, R. & Díaz García, F.). *Geological Society of America Special Paper*, **364**, 105–124.
- Santos Zalduegui, J.F., Schärer, U. & Gil Ibarguchi, J.I., 1995. Isotope constraints on the age and origin of magmatism and metamorphism in the Malpica Tui allochthon, Galicia, NW Spain. *Chemical Geology*, **121**, 91–103.
- Smye, A.J., Greenwood, L.V. & Holland, T.J.B., 2010. Garnet-chloritoid kyanite assemblages: eclogite facies indicators of subduction constraints in orogenic belts. *Journal of Metamorphic Geology*, **28**, 753–768.
- Stern, R.J., 2005. Evidence from ophiolites, blueschists, and ultra high pressure metamorphic terranes that the modern episode of subduction tectonics began in Neoproterozoic time. *Geology*, **33**, 557–560.
- Tracy, R.J., 1982. Compositional zoning and inclusions in metamorphic minerals. In: *Characterization of metamorphism through mineral equilibria* (ed Ferry, J. M.), Reviews in Mineralogy, Vol. 10, pp. 355–397, Mineralogical Society of America, Washington, DC.
- Wei, C. & Powell, R., 2003. Phase relations in high-pressure metapelites in the system KFMASH (K₂O-FeO-MgO-Al₂O₃-SiO₂-H₂O) with application to natural rocks. *Contributions to Mineralogy and Petrology*, **145**, 301–315.
- Wei, C.-J. & Song, S.-G., 2008. Chloritoid glaucophane schist in the north Qilian orogen, NW China: phase equilibria and *P-T* path from garnet zonation. *Journal of Metamorphic Geology*, **26**, 301–316.

- White, R.W., Powell, R., Holland, T.J.B. & Worley, B., 2000. The effect of TiO₂ and Fe₂O₃ on metapelitic assemblages at greenschist and amphibolite facies conditions: mineral equilibria calculations in the system K₂O FeO MgO Al₂O₃ SiO₂ H₂O TiO₂ Fe₂O₃. *Journal of Metamorphic Geology*, **18**, 497-511.
- White, R.W., Powell, R. & Clarke, G.L., 2002. The interpretation of reaction textures in Fe rich metapelitic granulites of the Musgrave Block, central Australia: constraints from mineral equilibria calculations in the system K₂O FeO MgO Al₂O₃ SiO₂ H₂O TiO₂ Fe₂O₃. *Journal of Metamorphic Geology*, **20**, 41-55.
- White, R.W., Pomroy, N.E. & Powell, R., 2005. An in-situ metatexite diatexite transition in upper amphibolite facies rocks from Broken Hill, Australia. *Journal of Metamorphic Geology*, **23**, 579-602.